Received: 28 August 2022 | Revised: 10 January 2023 | Accepted: 13 February 2023

DOI: 10.1002/hipo.23517

RESEARCH ARTICLE

WILEY

Organization of projections from the entorhinal cortex to the hippocampal formation of the Egyptian fruit bat *Rousettus aegyptiacus*

Bente Jacobsen[1,2] | Heidi Kleven[1,3] | Wairimu Gatome[2] | Liora Las[2] | Nachum Ulanovsky[2] | Menno P. Witter[1]

[1]Faculty of Medicine and Health Science, Kavli Institute for Systems Neuroscience, NTNU Norwegian University for Science and Technology, Trondheim, Norway

[2]Department of Brain Sciences, Weizmann Institute of Science, Rehovot, Israel

[3]Neural Systems, Institute of Basic Medical Sciences, UiO University of Oslo, Oslo, Norway

Correspondence
Menno P. Witter, Kavli Institute for Systems Neuroscience, NTNU Norwegian University for Science and Technology, Trondheim, Norway.
Email: menno.witter@ntnu.no

Funding information
H2020 European Research Council, Grant/Award Number: ERC-StG - NEUROBAT; Kavli Foundation; Kimmel Award for Innovative Investigation; Norwegian Research Council, Grant/Award Number: 223262

Abstract

The hippocampal formation and entorhinal cortex are crucially involved in learning and memory as well as in spatial navigation. The conservation of these structures across the entire mammalian lineage demonstrates their importance. Information on a diverse set of spatially tuned neurons has become available, but we only have a rudimentary understanding of how anatomical network structure affects functional tuning. Bats are the only order of mammals that have evolved true flight, and with this specialization comes the need to navigate and behave in a three dimensional (3D) environment. Spatial tuning of cells in the entorhinal-hippocampal network of bats has been studied for some time, but whether the reported tuning in 3D is associated with changes in the entorhinal-hippocampal network is not known. Here we investigated the entorhinal-hippocampal projections in the Egyptian fruit bat (*Rousettus aegyptiacus*), by injecting chemical anterograde tracers in the entorhinal cortex. Detailed analyses of the terminations of these projections in the hippocampus showed that both the medial and lateral entorhinal cortex sent projections to the molecular layer of all subfields of the hippocampal formation. Our analyses showed that the terminal distributions of entorhinal fibers in the hippocampal formation of Egyptian fruit bats—including the proximo-distal and longitudinal topography and the layer-specificity—are similar to what has been described in other mammalian species such as rodents and primates. The major difference in entorhinal-hippocampal projections that was described to date between rodents and primates is in the terminal distribution of the DG projection. We found that bats have entorhinal-DG projections that seem more like those in primates than in rodents. It is likely that the latter projection in bats is specialized to the behavioral needs of this species, including 3D flight and long-distance navigation.

KEYWORDS
comparative anatomy, hippocampal formation, parahippocampal region, perforant pathway, topographical organization

Bente Jacobsen and Heidi Kleven contributed equally to this article.

1 | INTRODUCTION

The ability to learn and form new memories depends heavily on the complex connections between the hippocampal formation (HF) and overlying entorhinal cortex (EC) (Moser et al., 2015; Ritchey et al., 2015; van Strien et al., 2009; Witter, Doan, et al., 2017). Projections from EC constitute the main cortical input to HF, and conversely most of the HF output reaches the cortex through EC. The importance and capabilities of the EC–HF network are perhaps the reason why these structures are so impressively conserved across the entire mammalian lineage. Although the structures and their connections are conserved, they are however not identical between all species (Witter, Kleven, et al., 2017). Hence, there are modifications to this system that likely tailor it to the needs of the individual species.

Many different cytoarchitectural divisional schemes for EC have been proposed that apply to different species or even to the same species (for the rat, see Insausti et al., 1997 and for the human and an extensive comparative description see Šimić et al., 2022); and even in bats, one scheme proposed five divisions of EC (Gatome et al., 2010). Functionally though, there seems to be a consensus that EC can be divided into two parts, and that these functional parts correspond largely to two cytoarchitectonically defined areas, the medial and lateral EC (MEC and LEC, respectively). This suggests that MEC and LEC provide HF with different types of information relevant for forming new memories (Keene et al., 2016; Witter, Doan, et al., 2017). Specifically, MEC in rodents, harbors cells that display allocentric spatial tuning, such as grid cells, border cells, object vector cells, and head direction cells (Hafting et al., 2005; Høydal et al., 2019; O'Keefe & Dostrovsky, 1971; Savelli et al., 2008; Solstad et al., 2008). In contrast, LEC contains cells that are tuned to objects, traces of objects or temporal sequences within events (Deshmukh & Knierim, 2011; Tsao et al., 2013, 2018). Both MEC and LEC feed information into the HF network through two largely segregated pathways, the medial and lateral perforant pathway. However, the exact purpose of keeping this information separate, and the way in which the information is integrated at the level of HF, remain unresolved.

Bats are the only order of mammals that have evolved true flight. This provides the opportunity to study behavior and neural signaling in three dimensions (3D), and to compare this to animals that essentially navigate in two dimensions, like rodents. On the functional level, we know that bats also have many of the spatially modulated cell types described in HF and MEC of rodents (Finkelstein et al., 2015, 2016; Ginosar et al., 2021; Yartsev et al., 2011; Yartsev & Ulanovsky, 2013). These studies further show how adding a third dimension impacts neural signaling and coding. Thus, place cells in bats navigating in 3D show spherical place-fields rather than a columnar structure. Further, 3D grid cells in the MEC of flying bats exhibit spherical firing-fields, but the arrangement of these fields does not follow a perfect global lattice, that is, does not exhibit a perfect 3D hexagonal grid; rather, 3D grid cells in bats show a local distance scale, implying a local metric for space, rather than a global metric. However, we do not know whether these changes in functional tuning are associated with a change in the connectional structure of the underlying network. Since we still have limited understanding of the structure–function relationships in the mammalian EC–HF network, taking a comparative approach by including the bat could lead to the identification of new principles underlying such structure–function relationships.

Although the anatomy and connections of the EC–HF system in rodents and certain other mammalian species are well described (van Strien et al., 2009; Witter, Doan, et al., 2017; Witter, Kleven, et al., 2017), there are only few studies that shed light on the structural and connectional anatomy of the EC–HF system in the bat brain (Buhl & Dann, 1991; Cotter & Laemle, 1990; Gatome et al., 2010). More specifically, there are no anatomical studies on the organization of the EC–HF projections. Hence, we decided to investigate the anatomical projections from EC to HF in the brain of the Egyptian fruit bat (*Rousettus aegyptiacus*) to complement the functional data that are already available in this species. To this end, we injected chemical anterograde tracers into MEC and LEC in the Egyptian fruit bat brain and performed detailed analyses of the terminations of these projections in the different subfields of HF. We report that the projections to most HF subfields showed distribution patterns and topographies similar to those in the rodent, but we also discovered that the terminal distributions in the dentate gyrus (DG) of HF, are slightly different compared to what has been described in rodents, and interestingly more like what has been shown in primates.

2 | METHODS

We used a total of 12 adult Egyptian fruit bats (*R. aegyptiacus*) of either sex for this study. The animals were collected as adults in the wild, examined by a veterinarian and then transferred to quarantine where they were kept for a month. After this period, the animals were brought to the laboratory facilities and housed in cages (2–5 bats per cage) in a temperature- and humidity-controlled room. All handling of animals and injections of tracers were performed at the Weizmann Institute of Science, and the experimental procedures were approved by the Institutional Animal Care and Use Committee and conform with EU directive 2010/63/EU on the protection of animals used for scientific purposes.

2.1 | Tracer injections

Prior to surgery, the bats received analgesia in accordance with their body weight (body weights 161–195 g at the time of surgery). The bats were then anesthetized by either an injection of a cocktail of ketamine 15 mg/kg and medetomidine 0.06 mg/kg or exposed to isoflurane in an induction chamber at 5% isoflurane for about 2 min. The anesthesia was maintained with isoflurane (0.25%–3%, as needed) in 98% oxygen throughout the surgery. The depth of anesthesia was monitored by testing toe pinch reflexes and observing the bats' breathing rates. Using a heating pad underneath the bat and a closed-loop temperature controller connected to a rectal temperature probe,

the body temperature was kept constant at approximately 35–36°C. After induction, the bats were placed in a stereotaxic frame (Kopf Instruments, Tujunga, CA) where the head position was fixed with ear bars. Using sterile procedures, the skull was exposed, and a small hole was drilled to expose the brain. Four different anterograde tracers: Biotinylated dextran amine 10 kDa (BDA, Thermo Fisher Scientific Cat# D1956, RRID:AB_2307337); Dextran, Alexa Fluor® 488, 10 kDa (DA 488, Thermo Fisher Scientific, Cat# D22910); Dextran, Alexa Fluor® 647 10 kDa (DA 647, Thermo Fisher Scientific, Cat# D22914); and Phaseolus vulgaris-leucoagglutinin (PHA-L; Vector Laboratories, Cat# L-1110, RRID:AB_2336656) were iontophoretically injected through a borosilicate-glass pipette with an outer tip diameter of 20–30 μm. We used a positive, pulsed direct current to inject the tracers (7 s on/7 s off, 6 μA for 17–30 min). In most cases, several injections were made in either one or both hemispheres of the brain, using different tracers. When the injection(s) were completed, the skull was cleaned with saline solution and the skin sutured. The bats received postoperative care for a period of 10 days and were treated with antibiotics for 7 days.

2.2 | Tissue collection and histology

Ten days postsurgery the bats were euthanized with an overdose of sodium pentobarbital, and then perfused transcardially first with 50 mL 0.9% phosphate buffer saline solution followed by 200 mL of fixative (4% paraformaldehyde + 0.1 M phosphate buffer saline). The brains were removed and postfixed in the same fixative at 4°C overnight. Subsequently, all brains were stored in a 30% sucrose solution at 4°C for a minimum of three nights before cutting. The brains were cut in 40 μm thick sections in either the coronal, horizontal, or sagittal plane on a freezing microtome (Microm HM430, Thermo Scientific, Waltham, MA) and collected in seven series that were either mounted directly on microscope slides (Superfrost Plus®, Gerhard Menzel GmbH, Braunschweig, Germany) with a Tris–HCl solution (0.606% Tris[hydroxymethyl]aminomethane in H_2O, pH adjusted with HCl to 7.6), or stored in a cryoprotective solution (20% glycerol, 2% DMSO diluted in 0.125 M) at −20°C for later histology. We used different planes of sectioning to prevent biased observations resulting from only looking at one plane. The distribution of fibers in the dorsal and ventral HF is best seen in coronal sections since these are oriented roughly perpendicular to the long axis. In the vertically oriented "intermediate" HF, horizontal sections are closer to the optimal perpendicular plane. Sagittal sections, in turn, are optimal to compare organizations along the complete long axis but are rather difficult for nonexperienced anatomists to interpret. The combination of all three planes allows for a thorough description of the spatial distribution of entorhinal axons in the HF.

2.3 | Cytoarchitecture

The tissue was stained either with cresyl violet or immunohistochemistry against the neuronal nuclear antigen (NeuN) to visualize cytoarchitecture. Cresyl violet staining was carried out on sections mounted on microscope slides. The sections were first dehydrated in graded ethanol baths (30%, 50%, 70%, 80%, 90%, and 96%), cleared in xylene (VWR International) and then rehydrated in ethanol baths (96%, 90%, 80%, 70%, 50%, and 30%) before they were stained in a cresyl violet solution (Sigma Aldrich, Cat# C5042-10g) for 5–10 min. The staining was differentiated by dipping the sections in a solution consisting of 70% ethanol and acetic acid (VWR International), and after this the sections were dehydrated and cleared in xylene before they were cover-slipped with Entellan™ (Sigma Aldrich). For staining against NeuN, we did immunohistochemistry on free floating sections. The sections were washed in 0.125 M phosphate buffer (PB) 4 × 10 min, before being permeabilized in PB containing 0.5% Triton X-100 (PBT; Sigma Aldrich) 2 × 10 min and preincubated in PBT containing 5% goat serum (Abcam, Cat# ab7481, RRID:AB_2716553) for 90 min, before being incubated over night at 4°C with primary antibody (Guinea pig anti-NeuN, Millipore, Cat# ABN90P, RRID:AB_2341095) 1:2000 concentration in PBT. The following day the sections were washed in PBT and incubated in secondary antibody (Goat anti-guinea pig AF647, Thermo Fisher Scientific, Cat# A-21450, RRID:AB_2735091) 1:400 in PBT, at room temperature. After incubation, sections were washed in PB 2 × 10 min, then in Tris–HCl for 20 min, and mounted with Tris–HCl on Superfrost Plus® microscope slides.

2.4 | Visualizing tracers

Brains injected with BDA had one series stained with 3,3′-diaminobenzidine tetrahydrochloride (DAB, Sigma Aldrich, Cat# D5905). The tissue was washed 3 × 10 min in PB, rinsed 2 × 10 min in H_2O_2 in methanol, washed again 3 × 10 min in PB, and permeabilized in Tris–HCl containing 0.896% NaCl and 0.5% Trition X-100 (TBS-Tx) before being incubated with in ABC solution (ABC kit, Vector Laboratories, Cat# PK-4000, RRID:AB_2336818). After the incubation, the sections were washed 3 × 10 min in TBS-Tx and 2 × 10 min in Tris–HCl after which they were stained with DAB. After DBA staining, the sections were washed 2 × 10 min in Tris–HCl and mounted with a 0.2% gelatine solution on microscope slides before being cover slipped with Entellan™. Another series from the same brain was stained using Strepdavidin, Alexa Fluor® 546 (Thermo Fisher Scientific, Cat# S-11225, RRID:AB_2532130). First, the tissue was washed 3 × 10 min in PB and 3 × 10 min in TBS-Tx, after this the tissue was incubated for 90 min in room temperature with Strepdavidin, Alexa Fluor® 546 (1:200) in TBS-Tx, before being washed 2 × 5 min in Tris–HCl mounted with a 0.2% gelatin solution on microscope slides and cover slipped with Entellan™ as the mounting medium.

One series from each brain injected with PHA-L was stained with an antibody against PHA-L (goat anti-PHA-L; Vector Laboratories, Cat# AS-2224, RRID:AB_2315136). For PHA-L staining the tissue was washed 3 × 10 min in PB, 3 × 10 min in H_2O_2/methanol, 3 × 10 min in PB, and permeabilized in TBS-Tx. After this the tissue was preincubated in 5% goat serum in TBS-Tx and washed 3 × 10 min in TBS-Tx

before incubation with the primary antibody, concentration 1:1000, for 48 h at 4°C. Subsequently, the tissue was washed 3 × 10 min in TBS-Tx and incubated for 1–2 h in room temperature with a secondary antibody (donkey anti-goat Alexa 488, Thermo Fisher Scientific, Cat# A-11055, RRID:AB_2534102) 1:100 in TBS-Tx. The tissue was then mounted with a 0.2% gelatin solution on microscope slides and cover slipped with Entellan™.

Sections obtained from brains injected with the tracers DA488 and DA647 were mounted, and cover-slipped directly after cutting.

2.5 | Data analysis

2.5.1 | Imaging

All materials were scanned using a Zeiss Mirax Midi Scanner, with a 20X, 0.8NA objective and either reflected fluorescent light or transmitted white light, or a Zeiss Axio Scan Z.1 scanner (Carl Zeiss MicroImaging GmbH, Jena, Germany). On the Axio scan, the sections were scanned with a Plan-apochromat 20×/0.8 NA M27 objective, a Colibri light source, quadruple filter and a Hamamtsu Ocra flash imaging device. For brightfield images, the same objective was used, and a Hitachi HV-F202SCL was the imaging device. Materials were analyzed and exported using the accompanying software (Mirax viewer 1.12 or Zen blue, ZEN Digital Imaging for Light Microscopy, RRID:SCR_013672). Any additional adjustments and cropping of images was done in Adobe Photoshop (RRID:SCR_014199).

2.5.2 | Delineation

We used Nissl and NeuN stained sections cut in the horizontal, coronal, and sagittal planes to identify the cytoarchitectural borders of the subfields and layers of HF and EC, as described in detail in the results. This formed the basis for the descriptions of locations of injections sites in the EC and for analyzes of the locations of axonal plexuses of the projections within the HF following EC injections.

2.5.3 | Analysis of injection sites

The injection sites were considered to be the entire area with tracer-filled cell bodies surrounding the scar from the glass micropipette. The size and position of each injection site varied. To illustrate the injection sites, we exported images from all sections containing part of an injection site from the scanner and superimposed them on the Nissl-stained section that most closely matched the core of the injection site. We delineated EC in all sections containing any part of an injection site to ensure that they were entirely contained within the EC and to determine if the whole injection was located within either the MEC or the LEC. The laminar coverage of each injection was evaluated based on observations of labeled somata; we did not make any attempt to quantify how much of each injection site was in each layer, but rather made qualitative observations since laminar coverage is known to impact the distribution of axonal labeling HF (van Strien et al., 2009).

2.5.4 | Analysis of projections

All delineations and terminal axonal fields in HF following EC injections were analyzed qualitatively by both first authors independently and, in case of discrepancies, evaluated by the last author. Delineations of hippocampal subfields and laminae were made based primarily on cytoarchitectural criteria, and the position of terminal axonal fields was marked in a spread sheet (Microsoft Excel, RRID:SCR_016137). We overlayed scans of sections with fibers with scans of Nissl stained sections from adjacent series and made sure that the HF or EC matched as closely as possible to make delineations of borders between subfields in HF and EC. In most cases, we were also able to use the autofluorescence in the sections to distinguish borders within the HF. A few representative cases were selected for illustrations of the typical distribution of axonal terminals in HF. All illustrations were made in Adobe Illustrator (Adobe Illustrator, RRID:SCR_010279) and Adobe Photoshop (Adobe Photoshop, RRID:SCR_014199).

2.5.5 | 3D reconstructions

3D reconstructions of the bat brain were made using the 3D reconstruction tool in Neurolucida 360 (Neurolucida, MBF, RRID:SCR_001775MicroBrightField). The brain outlines and subfields of HF and EC were traced in Nissl-stained sections from a coronally cut reference brain, and a 3D rendering was made using the 3D tool in Neurolucida 360. The outlines of the 3D structures were smoothened after the initial tracing. Injection sites were superimposed on the approximate coronal section where the core of each injection site was situated. The size of each injection site was not indicated in the 3D model.

3 | RESULTS

3.1 | Delineations of the EC and HF

The gross anatomy of the Egyptian fruit bat brain is similar to a rodent brain, with a smooth essentially nongyrated surface. Much like in rodents, EC is located on the posteroventral surface of the brain (Figure 1a), where it extends from the posterior and lateral portion of the rhinal fissure all the way down to the piriform lobe. Compared to the rodent EC, the bat EC takes up a slightly more ventral portion of the posterior cortical surface, but this difference is not very striking. The anatomical positioning of EC sets bat brains apart from the brains of carnivores and primates, where EC has moved medially and ventrally and is covered by the expanding temporal lobe. In all

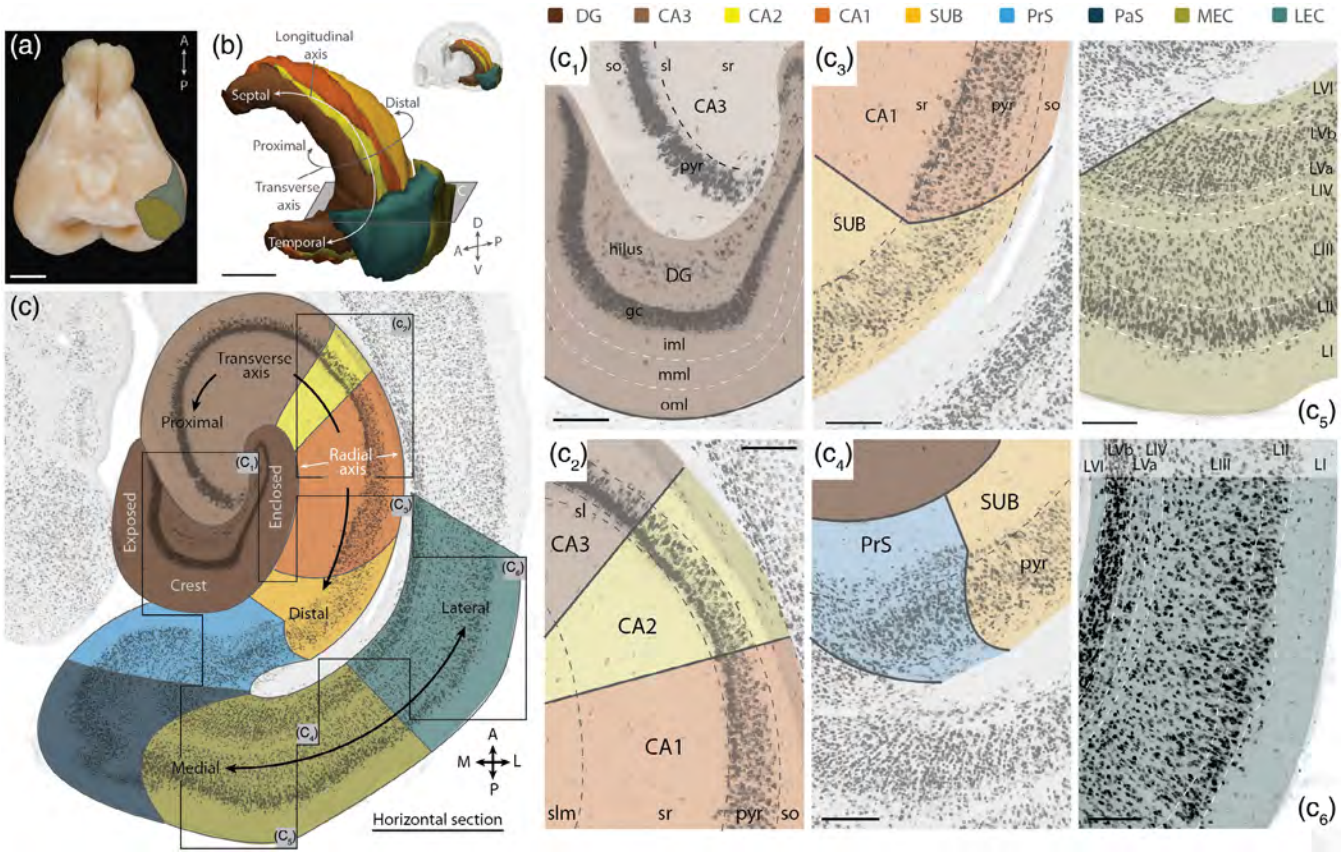

FIGURE 1 Overview of the hippocampal formation and entorhinal cortex in the Egyptian fruit bat. (a) Ventral view of an Egyptian fruit bat brain with the medial and lateral entorhinal cortices outlined on the brain surface (see color code in panel c; the color code applies to all panels). Scale bar, 4 mm. (b) 3D model of the bat HF and EC showing the different axes of the structure. Inset (upper right) shows the outline of the brain around HF and EC. Scale bar, 2 mm. (c) Horizontal section through HF and EC. Cytoarchitecture shown by immunohistochemistry against the neuronal nuclear antigen – NeuN. The positions of c_1–c_6 are indicated by the dimmed rectangles. Scale bar, 1000 μm. (c_1–c_6) Cytoarchitecture (NeuN), borders, and laminar delineations of the DG, CA3-1, SUB, MEC, and LEC. Scale bars, 200 μm. A, anterior; P, posterior; D, dorsal; V, ventral; M, medial; L, lateral; MEC, medial entorhinal cortex; LEC, lateral entorhinal cortex; DG, dentate gyrus; SUB, subiculum; so, *stratum oriens*; pyr thumblayer; iml, inner molecular layer; mml, middle molecular *layer*; oml, outer molecular layer. In c_5 and c_6 LI to LVI indicate the six layers of EC.

mammals investigated to date, including bats, HF is located directly adjacent to EC, and in bats and rodents, HF sits anterior and medial to EC, forming a curved cylindrical structure that spans almost the entire dorsoventral extent of the brain (Figure 1b and Figure S1).

Using cytoarchitectural criteria, we delineated EC and HF from surrounding cortices (Figure 1c and Figure S2) and distinguished the different subfields of the two structures. We based our delineations on literature from other mammals, on previous work done in other bat species, and on the Egyptian fruit bat stereotaxic brain atlas (see Eilam-Altstadter et al., 2022 for a detailed description of cytoarchitectonic features of all HF and EC subfields in the Egyptian fruit bat). In short, HF in the Egyptian fruit bat, as in all mammalian species, is a three-layered cortex with a superficial molecular layer, a central principal cell layer and a deep polymorphic layer (Figure 1c,c_1–c_4 and Figure S2). The laminar axis of HF is typically referred to as the radial axis, the transverse axis as the proximo-distal axis, and the longitudinal axis as the septotemporal axis (van Strien et al., 2009; Figure 1b,c). We further divided HF into the conventional five subfields—the DG, the CA3, CA2, and CA1 and the subiculum (SUB) (Figure 1c,c_1–$c_4$and Figures S2 and S3). The DG is the most proximal subfield of HF, it has a characteristic "U" shape both in coronal and horizontal sections (Figure 1c,c_1 and Figure S3a–d). There are several nomenclatures used to describe the components of DG, here we refer to the portion of the DG facing the HF and overlying cortex as the enclosed blade, and the opposing side facing subcortical structures as the exposed blade; the two blades are joined together at the "crest" (Figure 1c and Figure S2). Along the radial axis of DG, the molecular layer is typically divided into three parts: the inner, middle, and outer molecular layer (IML, MML, and OML, respectively). The inner molecular layer (IML) can be generally differentiated in any sectional plane based on its slightly more inhomogeneous appearance than the remaining outer part (Amaral & Lavenex, 2007). This latter portion looks very homogeneous in Nissl and NeuN stains, and therefore we divided the outer portion, for descriptive purposes only, into two approximately equal portions along the radial

axis, MML and OML (Figure 1c,c$_1$). Directly below the inner molecular layer there was a narrow densely packed layer of granule cells, the principal cells of DG. Deep to the granule cell layer there was a polymorphic layer, the "hilus," with large, loosely packed cells (Figure 1c,c$_1$). CA3 extended out of the DG polymorphic layer and wrapped back around the enclosed blade of DG (Figure 1c,c$_1$and Figure S3). The molecular layer of CA3 was divided into the superficial *stratum lacunosum-moleculare* (SLM) and the deeper *stratum radiatum* (SR); these sublayers were also present throughout the rest of the CA subfields. Additionally, the CA3 had a narrow lighter layer sitting right at the base of the principal cell apical dendrites, this was the *stratum lucidum* (SL) and is known to be the region where DG granule cells synapse onto the pyramidal principal cells of CA3 (Amaral & Lavenex, 2007) (Figure 1c,c$_1$,c$_2$). The pyramidal cells in CA3 were large, stained very dark in NeuN staining and they were densely packed together (Figure 1c$_1$,c$_2$ and Figure S3). The border to the CA2 could be recognized by the disappearance of the SL, and by a heterogenization of the pyramidal cells into two layers; a superficial layer with larger darkly stained cells and a deeper layer consisting of smaller, loosely packed cells that also had a lighter NeuN stain (Figure 1c,c$_2$ and Figure S3e–h). As CA2 transitioned into CA1 distally, the pyramidal cell layer became more homogenous, the larger superficial cells were lost, and small round loosely packed pyramidal cells filled a wider principal cell layer throughout CA1 (Figure 1c,c$_2$,c$_3$ and Figure S3e–h). The appearance of the CA1 pyramidal cell layer in the Egyptian fruit bat—which is wider and less densely packed than CA2 and CA3 – differs from that in rodents, where the CA1 pyramidal cells are typically more densely packed than in CA2. Hence, the appearance of the CA1 pyramidal cell layer in our data was more like what has been described in primates (Amaral & Lavenex, 2007). The border between CA1 and SUB was marked by a change in morphology among the pyramidal cells, going from a round shape of cell bodies in the CA1 to a more elongated shape in the SUB (Figure 1c,c$_3$, and Figure S4a–d). Moreover, the pyramidal cells in SUB typically had a lighter stain and appeared less organized than in CA1. SUB was also marked by a disappearance of the SO, and a narrowing of the molecular layer due to the disappearance of SR (Figure 1c,c$_3$). Distally, SUB bordered the presubiculum and this border formed the transition from the three-layered cortex of HF to a six layered cortex. Hence, the border between SUB and presubiculum was evident due to the addition of new cell layers (Figure 1c,c$_4$ and Figure S4e–h).

In the Egyptian fruit bat, as in other species, EC is a six layered cortex with two cell-sparse layers (layers I and IV). The distinct sparsity of layer IV (LIV) cells, together with strikingly large layer II (LII) cells, made it easy to delineate EC from surrounding cortices (Figure 1c,c$_5$,c$_6$, and Figures S2 and S5). We also used cytoarchitectonic criteria to separate MEC from LEC (Figure 1c,c$_5$, c$_6$ and Figure S5). In MEC, layer I (LI) was a wide cell-sparse layer, whereas LII contained large, densely packed cells that stained dark with a NeuN stain. Layer III (LIII) was uniform, with smaller lightly stained cells, and deep to this layer was a clear LIV, the "lamina dissecans," with few neurons. Layer V (LV) could be divided into sublayer LVa with large lightly stained cells, and LVb with smaller cells that were stacked in columns radially. Layer VI (LVI) was only a few cells wide, it did not have a uniform appearance and merged with the underlying white matter (Figure 1c,c$_5$ and Figure S5e,g,i). Overall, LEC had a less ordered appearance than MEC (Figure 1c,c$_5$,c$_6$ and Figure S5d–i; particularly evident when comparing S5d and S5f to S5e and S5g). LI was still wide and cell sparse, and LII was narrow with large darkly stained cells. However, these cells occasionally mixed into both LI and LIII. In parts of LEC, LII formed two sublayers with a narrow cell free zone in between (not shown in Figure 1). LIII of LEC had smaller lightly stained cells, but the overall appearance of the layer was less uniform than LIII in MEC. LIV of the LEC was cell sparse, but in parts of the LEC it was so narrow that it was hard to differentiate it between LIII and LV. LV in LEC was narrower than in MEC, but still consisted of two sublayers. LVa had large cells, but laterally in LEC, this layer could be only a single cell wide. LVb had smaller cells, these were not organized in radial columns as seen in MEC, rather the small darkly stained cells were packed quite closely together, while LVI was very narrow and disorganized, and it mixed with the underlying white matter (Figure 1c,c$_6$ and Figure S5d,f,h). To delineate the border between MEC and LEC, we focused on identifying the differences in LII organization, and additionally looked for the patchy appearance of LIII in LEC, the more apparent LIV in MEC, and the radially oriented layer Vb cells in MEC. Note that all these criteria apply, irrespective of the plane of sectioning.

3.2 | Description of injection sites

For this study, we analyzed 19 anterograde tracer injections in 12 animals: 12 of the injections were placed in MEC, six injections were placed in LEC, and one injection was situated at the border between MEC and LEC (Figure 2a–c). Seven brains, containing 12 injections in nine hemispheres were cut in the coronal plane. Two brains, containing three injections in two hemispheres were cut in the horizontal plane, and three brains, containing three injections in three hemispheres were cut in the sagittal plane. The MEC cases were sectioned in either coronal, horizontal, or sagittal planes, whereas LEC cases where exclusively sectioned in the coronal plane. In MEC, half of our injections covered all six cortical layers (Figure 2d), and the injections were spread out across the anteroposterior and mediolateral axes of the MEC (Figure 2a–c,e). Hence, we were able to analyze the HF projections of neurons in all layers of the MEC and revealed the topographical organization of these projections. In LEC, unfortunately, our injections did not consistently cover all cortical layers, and we had lower coverage of LII and LI than in our MEC dataset (Figure 2d). We did however have a few cases with sufficient LII coverage to gain important insight into the projections of LII LEC neurons to HF in the bat brain. We also

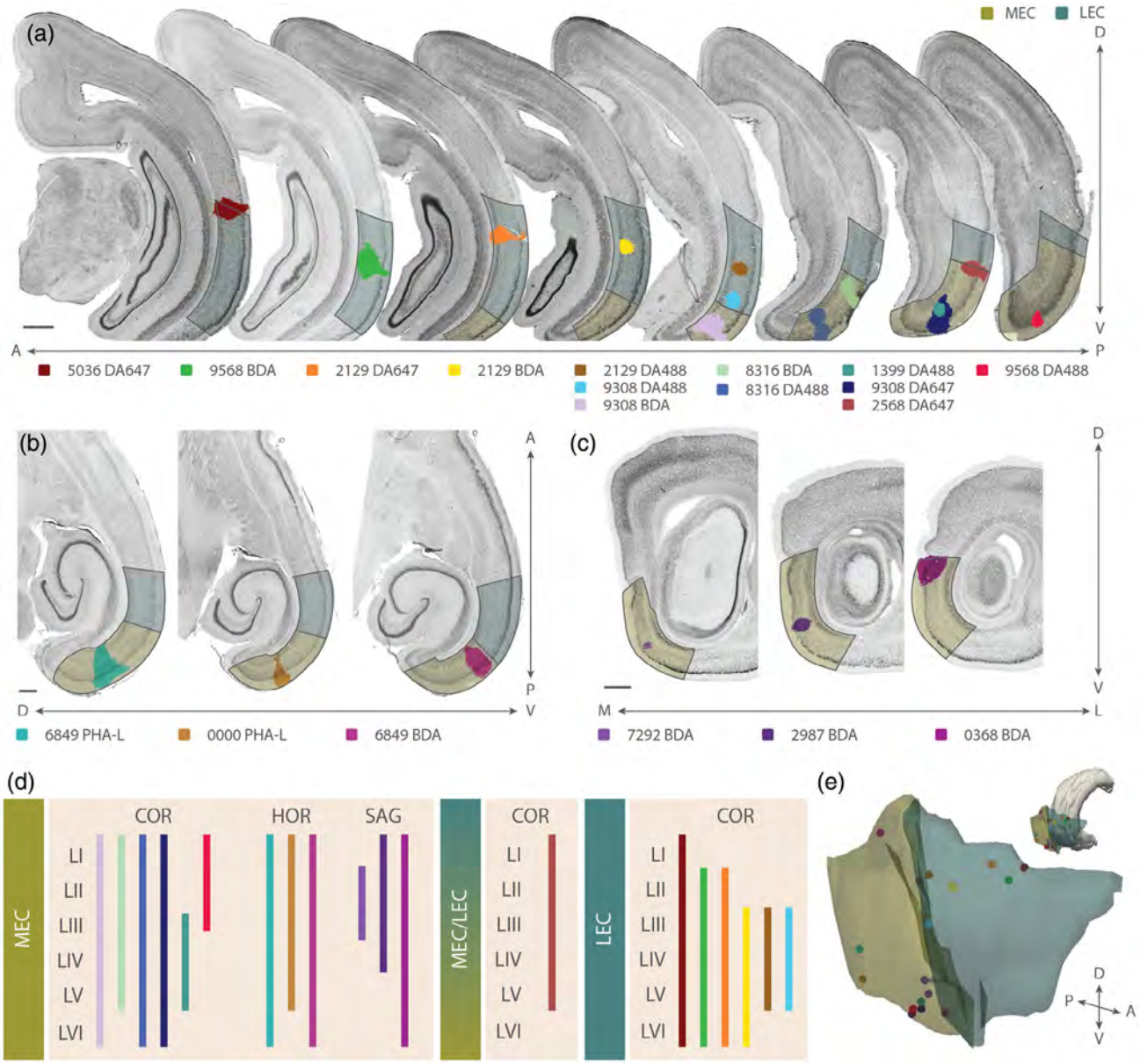

FIGURE 2 Position of injection sites and laminar coverage. (a) Coronal Nissl-stained sections showing the position of injection sites and delineations of the MEC and LEC overlayed (color code on upper right). Sections are organized from anterior to posterior, case numbers, and tracer types are color coded and indicated below. (b) Horizontal Nissl-stained sections with injection sites and delineations of the MEC and LEC overlayed. Sections are organized from dorsal to ventral, case numbers and tracer types are color coded and indicated below. (c) Sagittal NeuN stained sections with injection sites and delineations of the MEC overlayed, sections organized from medial to lateral, case numbers, and tracer types are color coded and indicated below. (d) Laminar coverage of the individual injections, colors correspond to colors in a to c. (e) 3D reconstruction of the MEC and LEC. Center of injection sites are indicated at their approximate mediolateral and dorsoventral positions. A, anterior; P, posterior; D, dorsal; V, ventral; M, medial; L, lateral; COR, coronal; HOR, horizontal; SAG, sagittal; MEC, medial entorhinal cortex; LEC, lateral entorhinal cortex. Scale bars, 500 μm.

had fair, though not complete, coverage of the dorsoventral and mediolateral axes of the LEC, which still allowed for the exploration of some of the topography of LEC projections to HF (Figure 2e). The single border case between MEC and LEC covered LI-V, the largest portion of the injection was situated in MEC and the LEC portion of the injection site touched mainly LIII, though a few LII cells were also included (Figure 2a, case 2568 DA647; and Figure 2d).

All injections resulted in labeling in HF ipsilaterally, though showing variable densities and terminal distribution patterns (Figure 3). Contralaterally only minor labeling was seen. Labeled axons followed the well-established routes to their target areas in HF (van Strien et al., 2009; Witter, 2007), that is, leaving EC through the deep white matter into the angular bundle and from there, crossing through the SUB at their point of entry along the long axis of HF, as well as traveling by way of the molecular layer of EC, through that of the para- and

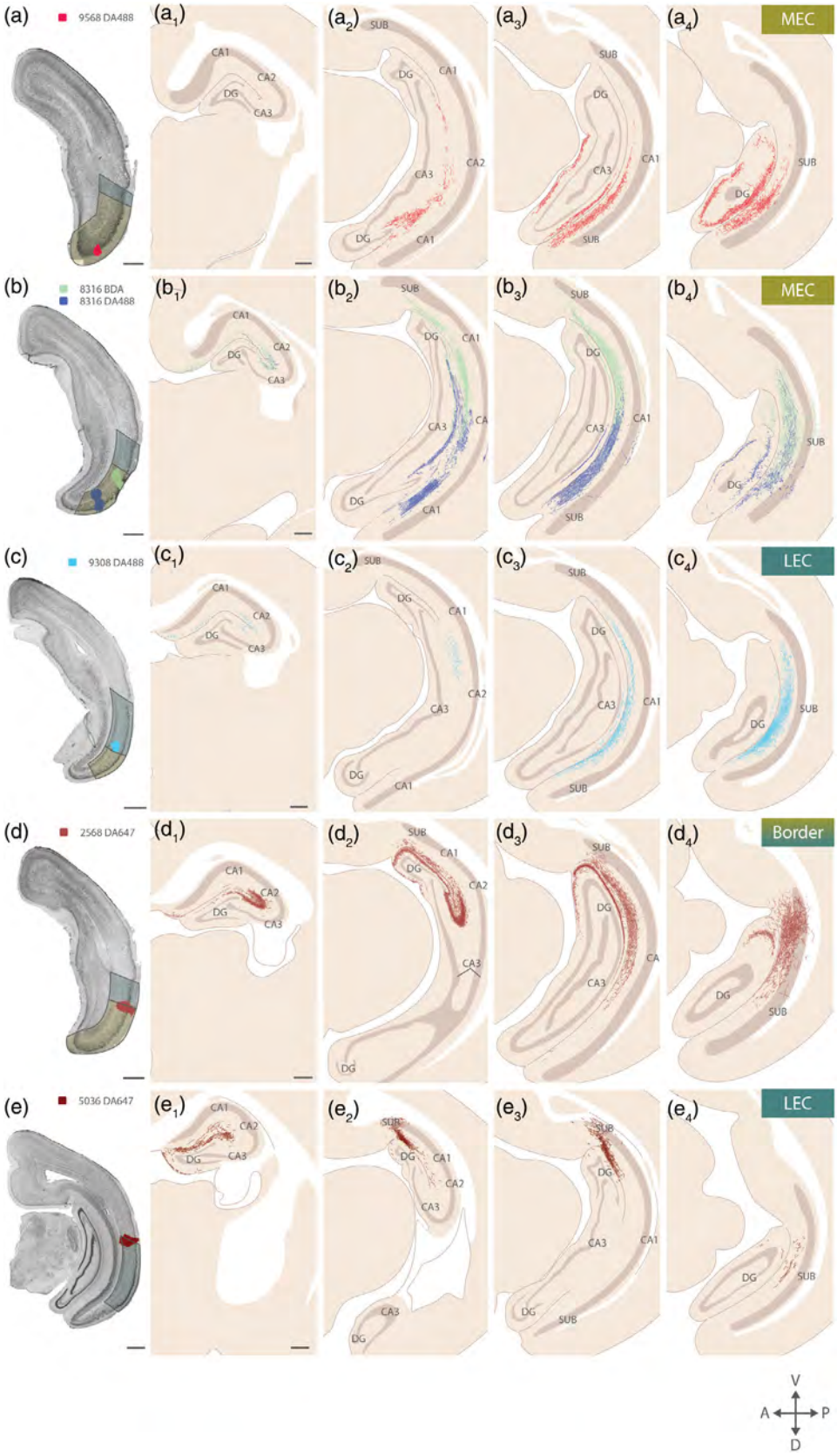

FIGURE 3 Overview of projections from the medial and lateral entorhinal cortices to the hippocampal formation in the Egyptian fruit bat. Examples of coronal sections through the hippocampal formation showing the overall organization of entorhinal projections to all subfields of the hippocampal formation and their longitudinal organization from septal to temporal hippocampal levels. Panels are organized with injection sites from ventral to dorsal cases (a–e), and illustrations of axonal termination patterns from anterior to posterior (1–4). Panels a and b show injections in the MEC, panels c and e show injections in the LEC, and panel d is an injection at the border between the MEC and LEC. Scale bars in a–e 1000 μm, scale bars in a_1–e_1 500 μm. MEC, medial entorhinal cortex; LEC, lateral entorhinal cortex; DG, dentate gyrus; SUB, subiculum. A, anterior; P, posterior; D, dorsal; V, ventral.

pre-subiculum, joining the previous component in the molecular layer of SUB. Axons either terminated there or crossed the hippocampal fissure to enter the molecular layer of DG. An additional contingent entered SLM of CA1, CA2, and CA3, and terminated there or continued to curve around the tip of the hippocampal fissure, reaching the molecular layer of DG.

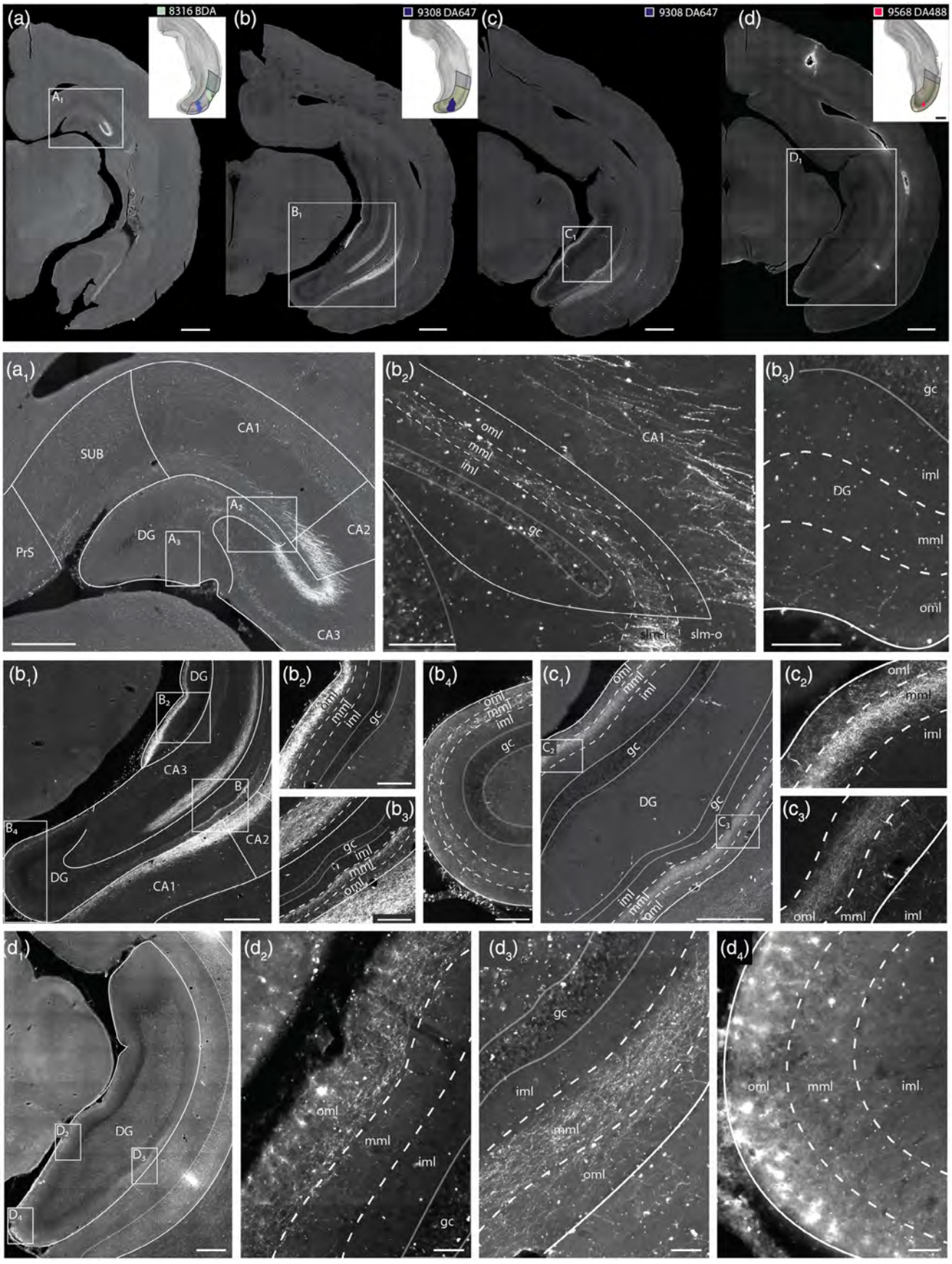

FIGURE 4 Legend on next page.

3.3 | Transverse and radial organization of projections

3.3.1 | Projections from the medial EC to the HF

Our data showed that neurons in MEC send substantial projections to all subfields of HF, this was consistent across all 12 MEC injections. Here, we show five representative MEC injections in detail that clearly summarize the findings in our data (Figures 3a,b, 4, and 5). In DG, the labeled projections terminated in the superficial two-thirds of the molecular layer (i.e., in MML and OML, Figures 4 and 5). Though there was an overall preference for MEC fibers to terminate in the MML, terminations in the OML were also common. The exact termination pattern of MEC fibers in DG differed between the enclosed and the exposed blades (Figures 4 and 5). In the enclosed blade, a robust narrow fiber plexus was present in all analyzed cases. This dense narrow plexus of MEC fibers was typically observed in MML (Figures 4a–a_2, b_1 and b_3, c_1 and c_3, d_1 and d_3 and 5). The plexus was at its narrowest at the border between CA3 and DG and widened gradually into the direction of the crest (Figures 4a_2 and 5a,b). In certain cases, sparse fibers were also present in the outer molecular layer, but this plexus was much less striking than the labeling in the middle molecular layer (Figure 4a_2,c_3,d_3). In contrast, the fiber plexus in the exposed blade was variable. First, a plexus in the exposed blade was sometimes very sparse compared to the enclosed blade in the same section, this was particularly noticeable in the dorsal HF (compare Figure 4a_2,a_3). Second, the plexus in the crest and exposed blade, did not maintain a fixed position in the molecular layer. Rather, it showed coverage of only the OML (Figure 4b_1,b_2), or it covered both the MML and OML (Figures 4c_1,c_2 and 5a,b) with varying labeling intensity. The position of the plexus in the crest and exposed blade even varied along the longitudinal axis of DG within the same injected case (Figure 4; compare b_2–c_1). We could not determine that the radial position of the plexus varied in a consistent manner relating to the position of the injection sites, hence it seemed that the organization of fibers in the exposed blade was without a distinct laminar topography, but still restricted to the OML and MML.

In CA3, MEC projections solely targeted SLM. The plexus widened and the labeling strength intensified compared with DG (Figure 5a,b). The plexus in SLM occupied the entire inner half of SLM proximally in CA3 but broadened as it entered CA2, and at the distal CA2 border the plexus covered the entire radial extent of SLM (Figure 5). This organization was most evident in horizontal sections through the HF (Figure 5a,b) and in anterior coronal sections through the dorsal HF (Figure 4a_1). Overall, the fiber labeling in CA2 was less dense than in CA3 (Figure 5).

In CA1, there was an increase in plexus density right at the border between CA2 and CA1, that is, in the proximal CA1, as seen in horizontal sections (Figure 5). Note the apparent drop in labeling intensity in CA1 in Figure 4a_1, which is a coronal section, where the CA1 adjacent to CA2 is positioned more ventrally in the HF, and thus overall receives less dense projections from the injected area in the MEC. As can be seen in Figure 5, the CA1 terminal plexus covered the radial extent of SLM, and the staining was very intense. This intense staining continued for a short distance distally before it decreased significantly in intensity, with individual axons showing more of the morphology associated with passing fibers. This type of labeling was maintained when crossing the border to SUB. There were no clear indications in the fiber plexus that the transition from CA1 to SUB happened. Distally in SUB, close to the presubiculum border, the plexus once again intensified to produce similar terminal labeling as that observed in proximal CA1 (Figure 5a,b). However, the plexus in SUB tended to show a somewhat smaller extent along the proximo-distal axis than in CA1.

3.3.2 | Projections from the lateral EC to the HF

Like the MEC cases, anterograde tracer injections in LEC gave rise to fiber labeling in all subdivisions of HF (Figures 3c,e, and 6). However,

FIGURE 4 Radial and proximodistal organization of medial entorhinal projections to the dentate gyrus. Coronal sections through the dentate gyrus at four different anterior–posterior/dorso-ventral levels (a–d), in three injected cases. Hippocampal subfields are delineated by solid lines, and sublayers of the molecular layer are delineated by dotted lines. White boxed areas indicate the positions of a_1, b_1, c, and d_1, respectively. Scale bars, 1000 μm. (a_1) Overview of an anterior section through the dorsal hippocampal formation, with positions of a_2 and a_3 marked (white rectangle). Scale bar, 500 μm. (a_2) Details of MEC to DG projection in the enclosed blade. Scale bar, 200 μm. (a_3) Details of MEC to DG projection to the outer molecular layer in the exposed blade of DG. Scale bar, 200 μm. (b_1) Delineations of hippocampal subfields in the intermediate hippocampal formation, and indication of the positions of b_2, b_3, and b_4 (white rectangles). Scale bar, 500 μm. (b_2) Details of MEC projections to the outer molecular layer in the exposed blade of the DG. Scale bar, 200 μm. (b_3) Details of MEC projections to the middle and outer molecular layer of the enclosed blade of the DG. Scale bar, 200 μm. (b_4) Details of MEC projections to the middle and outer molecular layer of the DG crest. Scale bar, 200 μm. (c_1) delineations of hippocampal subfields in a posterior section of the hippocampal formation, following the same injection as in b showing indication of the positions of c_2, and c_3 (white rectangles). Scale bar, 500 μm. (c_2) Details of MEC projections to the middle and outer molecular layer in the exposed blade of DG. Scale bar, 200 μm. (c_3) Details of MEC projections to the middle and outer molecular layer in the enclosed blade of DG. Scale bar, 200 μm. (d_1) delineations of hippocampal subfields in a posterior section of the DG, showing indication of the positions of d_2–d_4 (white rectangles). Scale bar 200 μm. (d_2) Details of MEC projections to the outer molecular layer of the exposed blade. (d_3) Details of projections to the middle and outer molecular layer of the enclosed blade. (d_4) Details of projections to the crest. gc, granule cell layer; iml, inner molecular layer; mml, middle molecular layer; oml, outer molecular layer; pyr, pyramidal cell layer; slm-i, stratum lacunosum moleculare inner; slm-o, stratum lacunosum moleculare outer; DG, dentate gyrus; PrS, presubiculum.

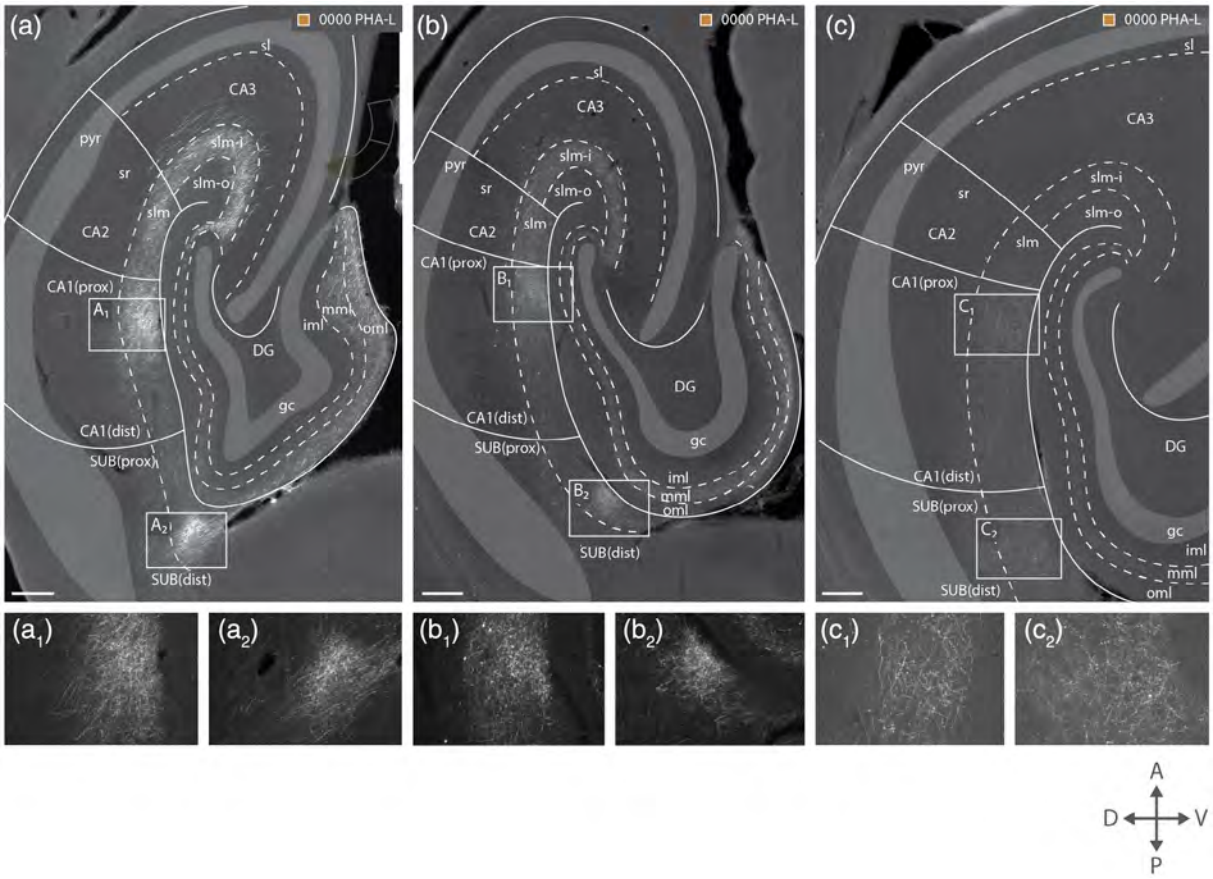

FIGURE 5 Radial and proximodistal organization of medial entorhinal projections to the hippocampal formation. Horizontal sections through the hippocampal formation at three different dorso-ventral levels (a–c) showing the radial and proximo-distal organization of MEC fibers across all hippocampal subfields. Hippocampal subfields are delineated by solid lines, and sublayers of the molecular layers are delineated by dotted lines. Inset in 'a' shows the injection site, and white boxes indicate areas that are shown in greater detail in a–c_1 and a–c_2 Fibers are evident in the mml and oml of the DG (a–c), in the slm-i of the CA3 (a and b), in the whole width of the slm in the CA2 (a and b), and in the proximal CA1 and distal SUB (a–c). Details of plexuses in proximal CA1 a_1–c_1. Details of distal SUB plexuses in a_2–c_2. All three sections are from case 0000 PHA-L: injection in intermediate MEC. Scale bars, 200 μm. DG, dentate gyrus; SUB, subiculum; gc, granule cell layer; iml, inner molecular layer; mml, middle molecular layer; oml, outer molecular layer; pyr, pyramidal cell layer; sl, stratum lucidum; sr, stratum radiatum; slm, stratum lacunosum moleculare; slm-i, slm-inner; slm-o, slm-outer; prox, proximal; dist, distal.

we consistently saw sparser labeling in DG and CA3/CA2 following LEC injections as compared to our MEC injections, while labeling in CA1/SUB was comparable between the two datasets (compare Figures 4 and 5 to 6). We attribute this difference to the laminar coverage of our LEC injections, where involvement of layer II was limited (Figure 2a,d). Layer II principal neurons have previously been shown to contribute most of the fibers that project to the DG and CA3/CA2 regions in rodents (Witter, 2007). Thus, this difference in labeling intensity probably does not demonstrate that projections from LEC to DG and CA3/CA2 are weaker than projections from MEC to the same regions, but rather is in line with the specific laminar origin of projections from EC to HF.

In the cases that showed DG labeling, we observed fibers in both OML and MML of the enclosed blade, the labeling was comparatively dense in the two sublayers of the molecular layer (Figure 6a,a_1 and d,d_1). Fibers in the exposed blade following LEC injections were very infrequent even if a labeled plexus in the enclosed blade and parts of the crest was evident. However, if fibers were present in the exposed blade, they were situated only in OML (not shown). As in the MEC cases, we were not able to determine any clear differences in injection topography between cases that showed fibers in the exposed blade and those that did not. Fiber labeling in CA3 and CA2 following LEC injections was, much like in DG, sparser than in the MEC cases. The plexus was shifted into the outer part of SLM in CA3, though some fibers in the inner half were also present (Figure 6b,b_1 and e,e_1), and the plexus widened to cover the complete radial width of SLM in CA2, like what was seen in case of injections in MEC (Figure 6b,b_1). Interestingly, the plexus in the CA2 of LEC cases was denser than the CA3 plexus, whereas in MEC cases the CA3 plexus was typically stronger than the CA2 plexus (compare Figures 5a,b to 6b,b_1). Overall, our data showed that CA3 projections from MEC and LEC had only a small radial overlap, whereas in CA2 these projections largely mixed.

Unlike the labeling in DG and CA3/CA2, we observed very strong fiber labeling in CA1 and SUB following LEC injections (Figures 3c,e

and 6c,c_1 and f,f_1). This likely indicates that, like what has been reported in rodents and primates, LEC injection sites covering LIII to VI include a large portion of the cells that project to CA1/SUB, while DG/CA3 projecting cells are likely confined to LII (Witter, Doan, et al., 2017; Witter, Kleven, et al., 2017). In terms of topography, projections from LEC terminated in the distal CA1 and proximal SUB—opposite to what we observed in MEC cases (compare Figures 5 to 6c,f). The LEC plexus in CA1 and SUB appeared to be continuous across the border between the two HF subfields, with no changes in the plexus width or intensity as it crossed from one subfield to the next (Figure 6c,f).

3.3.3 | Projections from the border region between the medial and lateral entorhinal cortices

In a single case, the injection site was located on the border between MEC and LEC (Figure 2a,d (case 2568 DA647) and Figure 3d). The

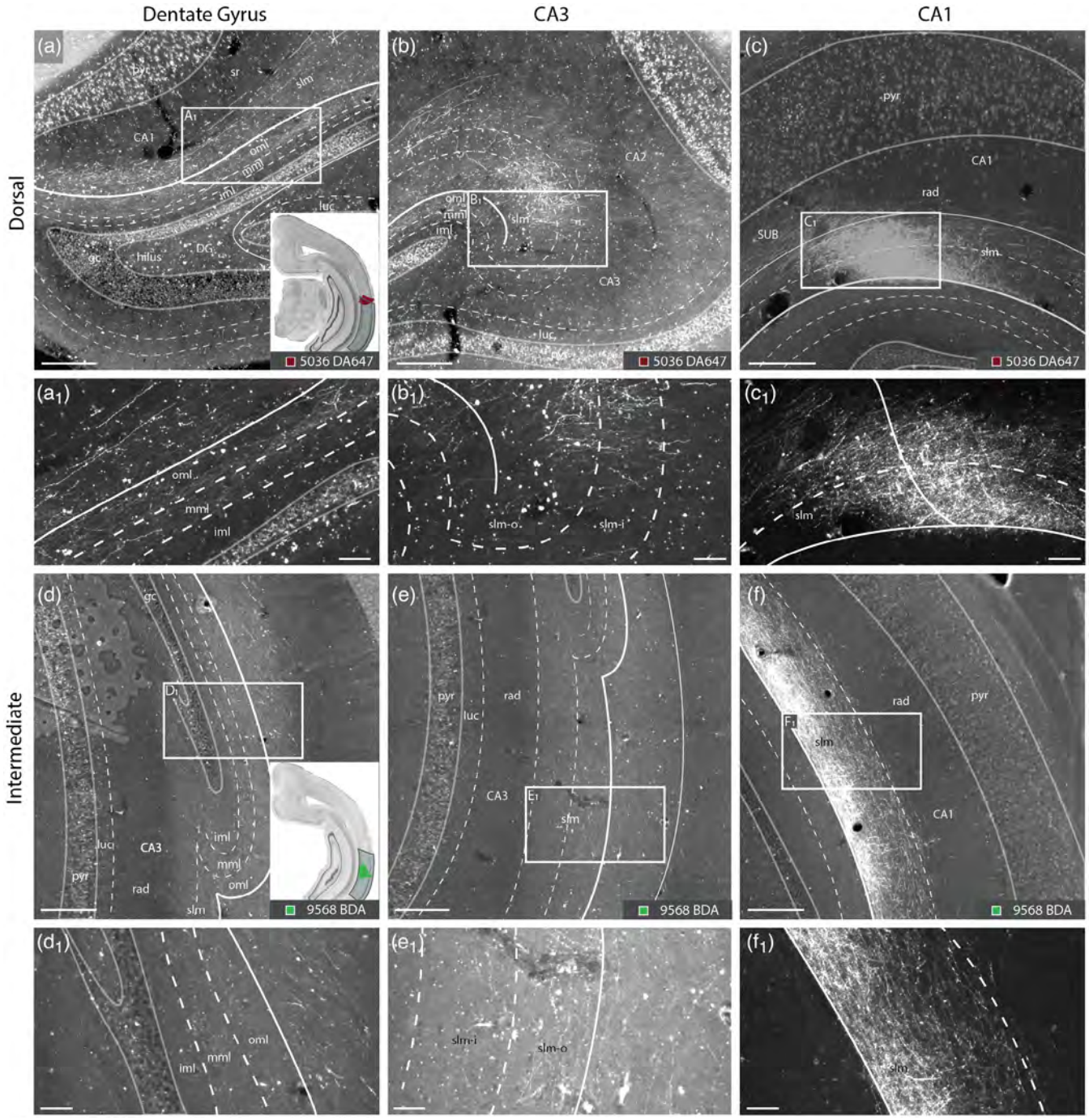

FIGURE 6 Legend on next page.

injection involved MEC more than LEC, and the LEC portion of the injection mainly involved layer III and IV, though a few cells in layer II were also labeled (Figure 2). In MEC, the injection covered layers I–Va. The injection thus involved an intermediate part of EC, and the resulting fiber plexus was present in dorsal and intermediate part of HF. The strongest plexus in DG was in MML in the enclosed blade, but it moved to OML in the crest and exposed blade (Figure 3d–d_4). There were also scattered fibers in OML in the enclosed blade. In CA3, much like in DG, the most prominent plexus was found in the inner SLM, but fibers were also clear in the outer half of SLM, suggesting contributions from both MEC and LEC projection neurons. In CA1 and SUB, there was a strong plexus that resembled the typical MEC proximo-distal distribution, that is, present in the proximal CA1 and the distal SUB. However, there were fibers also in the parts of the distal CA1 and adjacent proximal SUB, which are typically targeted by LEC projections.

3.4 | Longitudinal organization of projections

Although all anterograde injections resulted in labeled axons in HF, these axons never reached the full longitudinal or septotemporal extent of HF. The spread along the longitudinal axis depended on the position and the size of the injection, such that injections in ventral, intermediate, and dorsal EC resulted in labeled fibers in the temporal, intermediate and septal levels of HF, respectively (Figure 3). For both DG and CA3/CA2, it was clear that dorsal injections in MEC produced strong labeling in the septal DG and CA3/CA2, and the plexus moved gradually toward the temporal tip of these structures as the injections were placed more ventrally in MEC (Figure 3a,b; compare injection 8316 BDA to injection 8316 DA488 in Figure 3b–b_3). The LEC injections showed a similar dorsoventral pattern, with a dorsal LEC injection resulting in septal labeling in HF and a more ventral injection giving rise to labeling in the intermediate HF (compare Figure 3e,c). Hence, the classical mammalian longitudinal topography was evident and consistent in the projections from both entorhinal subdivisions in the bat.

4 | DISCUSSION

We used anterograde tracer injections in MEC and LEC to investigate the EC–HF connectivity in the Egyptian fruit bat. Our data show that both entorhinal subdivisions send projections to the molecular layer of all HF subfields (Figures 3 and 7). Projections to DG originating from both LEC and MEC targeted the outer two-thirds of the molecular layer. Projections from the MEC to the DG terminated in both the enclosed and exposed blades of DG, but projections to the enclosed blade were more prominent. Moreover, projections to the enclosed blade tended to terminate more densely in the MML than in the OML whereas in the exposed blade the terminations were variable in both the MML and OML. Projections from the LEC, on the other hand, terminated primarily in the enclosed blade but targeted both the MML and OML. A few terminations were also seen in the exposed blade, these were exclusively located in the OML. Our data thus show that there is a substantial radial overlap between terminations from the MEC and LEC in DG of the Egyptian fruit bat. The radial distribution of the projection from LII of EC to DG and CA3 is very well defined in rodents. Axons from MEC show a strong preference to target MML, and axons from LEC project preferentially to OML (van Groen et al., 2003; Witter, 2007; Witter, Doan, et al., 2017). A similar organization of EC to DG projections is described in the cat (Ino et al., 1998). In primates, however, the EC projections to DG have an organization where MEC and LEC fibers are mixed in both MML and OML with some variations along the longitudinal axis (Witter, 1989; Witter & Amaral, 1991). In conclusion, the radial distribution of EC-projections in the molecular layer of DG in the bat is most comparable to that seen in primates (Figure 7). Surprisingly, the pattern in CA3 of the fruit bat is strikingly different, with projections from MEC mainly targeting the inner half of SLM and those coming from LEC terminating preferentially in the outer half of SLM, though we often observed sparse labeling in the inner SLM of CA3 following LEC injections. This distribution appears much more like what has been reported in rodents (Hjorth-Simonsen, 1972; Hjorth-Simonsen & Jeune, 1972; Wyss, 1981) and different from that in primates (Witter & Amaral, 1991).

FIGURE 6 Radial and proximodistal organization of lateral entorhinal projections to the hippocampal formation. Coronal sections through the hippocampal formation at four different anterior–posterior/dorsoventral levels, showing lateral entorhinal terminations in the different subfields of the hippocampal formation. Hippocampal subfields are delineated by solid lines, while sublayers of the molecular layers are delineated by dotted lines. (a–c) Data from an injection in dorsal LEC. (d–f) Data from an injection in intermediate LEC. (a) Part of the anteriodorsal hippocampal formation showing MEC terminals in the DG and CA1. Scale bar, 500 μm. (a_1) Details (rectangle in a) from the molecular layer of the DG and the slm of the CA1. Scale bar, 500 μm. (b) Part of the anteriodorsal hippocampal formation showing MEC terminals in the CA3 and CA2. Scale bar, 500 μm. (b_1) Details (rectangle in b) form the slm of the CA3/CA2. Scale bar. (c) Part of the dorsal hippocampal formation showing MEC terminals in the border region between the CA1 and SUB. Scale bar, 500 μm. (c_1) Details (rectangle in c) form the slm of the CA1/SUB. (d–f) Data from and injection in the intermediate LEC. (d) Part of the intermediate hippocampal formation showing MEC terminals in the molecular layer of the DG. Scale bar, 500 μm. (d_1) Details (rectangle in d) from the molecular layer of the DG. Scale bar, 500 μm. (e) Part of the intermediate hippocampal formation showing sparse MEC terminals in the slm of the CA3. Scale bar, 500 μm. (e_1) Details (rectangle in e) from the slm of the CA3. (f) Part of the intermediate hippocampal formation showing MEC terminals in the slm of the CA1 and SUB. Scale bar, 500 μm. (f_1) Details (rectangle in f) from the molecular layer of the DG. Scale bar, 500 μm. Scale bar, 500 μm. Scale bar. DG, dentate gyrus; SUB, subiculum; gc, granule cell layer; iml, inner molecular layer; mml, middle molecular layer; oml, outer molecular layer; pyr, pyramidal cell layer; luc, stratum lucidum; rad, stratum radiatum; slm, stratum lacunosum moleculare; slm-i, slm inner; slm-o, slm outer; prox, proximal; dist, distal.

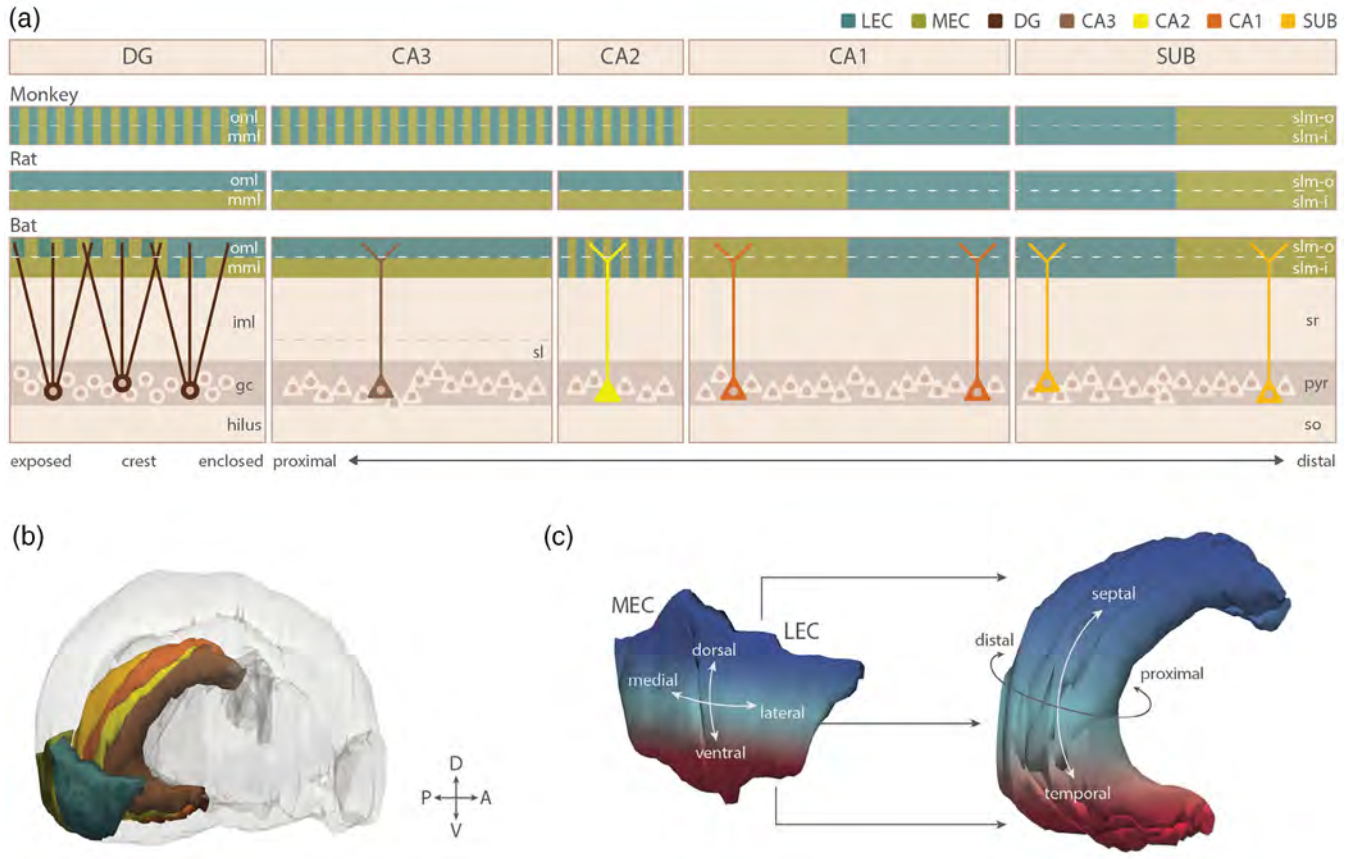

FIGURE 7 Summary of projections from the entorhinal cortex to the hippocampal formation in the bat brain, and comparison with other species. (a) Schematic summary of entorhinal projection patterns in the hippocampal formation of monkeys, rats, and bats. The hippocampal subfields are organized from proximal to distal, and fibers from the medial and lateral entorhinal cortices are color coded in the molecular layer of the dentate gyrus and the *stratum lacunosum moleculare* of the CA3-1 and SUB (color code of entorhinal fiber origin and hippocampal targets is shown on top right). (b) Anterolateral view of a 3D model of the bat brain with the hippocampal formation and entorhinal cortex and their subdivisions, color-coded. (c) Topographic organization of projections from the entorhinal cortex, now shown as a flattened representation of the full 3D extent (see panel b) to the hippocampal formation in the bat: the dorso-ventral axis of EC topographically maps onto the dorso-ventral (septo-temporal) axis of the hippocampal formation. Note that the dorso-ventral topographic organization we found in the bat appears similar to that observed in all mammalian species studied thus far, including primates and rodents, though the orientation of the dorsoventral axis in the bat seems less tilted than In other species, where this axis is generally described as having a dorsolateral-to-ventromedial orientation. DG, dentate gyrus; SUB, subiculum; MEC, medial entorhinal cortex; LEC, lateral entorhinal cortex; A, anterior; P, posterior; D, dorsal; V, ventral; gc, granule cell layer; iml, inner molecular layer; mml, middle molecular layer; oml, outer molecular layer; pyr, pyramidal cell layer; sl, stratum lucidum; sr, stratum radiatum; slm, stratum lacunosum moleculare; slm-i, slm inner; slm-o, slm outer.

Interestingly, projections from both entorhinal subdivisions seem to innervate SLM of CA2 in an overlapping pattern showing no clear preference for a more outer versus a more inner innervation along the apical dendrites in SLM, nor showing a preferred location along the transverse or proximodistal axis in CA2. The projections from LEC to CA2 were comparatively denser than those from MEC. This is of interest in view of the overall weaker labeling we observed of projections from LEC to DG and CA3. We attributed this sparsity in DG and CA3 to the limited labeling of LEC layer II neurons in our LEC injections, but this denser CA2 projection following LEC injections does not support this, since the latter projection is also known to originate from neurons in layer II (Witter, 2007). This obviously needs to be revisited, and retrograde tracing will likely help to resolve this apparent discrepancy.

When it comes to the organization of projections from MEC and LEC to the CA1 and SUB, there was a marked topographical organization along the transverse axis. While MEC sent projections to the proximal CA1 and distal SUB, projections from LEC targeted the distal CA1 and proximal SUB (Figure 7)—the same proximodistal topography as found in rodents and primates (Naber et al., 2001; Tamamaki & Nojyo, 1995; Witter & Amaral, 1991).

Overall, our data thus show that many features of the EC projection patterns in HF of the Egyptian fruit bat strongly resemble patterns described in nonprimate species and nonhuman primates (Ino et al., 1998; Tamamaki, 1997; Tamamaki & Nojyo, 1993; van Groen et al., 2003; Witter, 1989, 2007; Witter et al., 1989; Witter, Doan, et al., 2017; Wyss, 1981), and even the limited data in humans on EC-SUB projections (Maass et al., 2015).

The implication of keeping projections from MEC and LEC in separate laminae in DG is that the inputs will terminate on different segments of the granule cell dendrites. Hence, in rodents the LEC inputs will preferentially target distal apical dendrites, and the MEC inputs will target more proximal parts of these dendrites of principal neurons in DG and CA3. This may possibly position inputs from MEC and LEC to interact in a way that is different from when these EC fibers are mixed, like we see in both bats and primates. One intriguing example comes from reports that in rodents the MEC-DG synapses exhibit a predisposition toward the expression of potentiation, whereas LEC-DG synapses prefer to express synaptic depression (Collitti-Klausnitzer et al., 2021). Although this functional difference seems associated with differences in receptor make-up, it is potentially possible that the more proximal versus more distal dendritic localization of the synaptic contacts is relevant in this context.

Interestingly, the distribution of MEC and LEC fibers along the proximo-distal axis in SLM of CA1 and the molecular layer in SUB is maintained across all species investigated to date, including the bat, as shown in the present study: in all species, inputs from the MEC and LEC target separate populations of neurons, differently located across the proximo-distal axis of CA1 and SUB. This implies that integration of these inputs would have to happen via network-level processing in CA1 and SUB, rather than on the individual postsynaptic cells as is the case in DG, CA3, and CA2. It remains unknown why this difference in integration across hippocampal subfields is important and how this specifies the functional role of neurons in the HF (Flasbeck et al., 2018; Nakamura et al., 2013). The data from multiple mammalian species do however emphasize the likely functional relevance of having a convergence of the lateral and medial perforant pathway layer II components on the population of neurons in DG and CA3/CA2, and at the same time separating the lateral and medial perforant pathway layer III components across distinctly different populations of neurons in CA1 and SUB. Since in all species studied so far, the origin and distribution of the reciprocal projections from CA1 and SUB reflects the same topographical organization across species (Amaral et al., 1991), we postulate that in the Egyptian fruit bat—as in other species—neurons in proximal CA1 will project to the distal SUB, and both neuron-populations will project to layer V of MEC. Likewise, neurons in distal CA1 in the bat will project to the proximal SUB, and both populations will project to layer V of LEC.

Summing up, the overall architecture of the Egyptian fruit bat EC–HF system is similar to all other mammalian species that have been investigated to date, including rodents and primates. Specifically, our tracing data show that the projections from EC to HF are largely preserved across species. The similarities include both the transverse (proximo-distal) topography of projections and the longitudinal (dorsoventral) topography. We further show some specializations between different mammalian species, specifically in the projections from superficial layers of the EC to the DG and CA3. Our findings on the structural organization of the projections from EC to HF in bats seem to point to a kind of hybrid situation, somewhere in between the rodent and primate organization. On the one hand, the EC-to-DG projections are a bit more primate-like, but on the other hand the EC-to-CA3 projections are more rodent-like. Although it has previously been suggested that parts of the bat order, including the Egyptian fruit bats, may share a common ancestor with primates, more recent evidence suggests that the orders are relatively distantly related (Pettigrew et al., 1989; Springer et al., 2004; Tsagkogeorga et al., 2013). Rather, bats share a more recent common ancestor with carnivores, cetaceans, and ungulates, while rodents are more closely related to primates on the phylogenetic tree—even though the neuroanatomy of the EC–HF projections places the fruit bat a bit closer to the primate. This indicates that similarities in the neuroanatomy of this network between the Egyptian fruit bats and primates might be an example of convergent evolution—meaning that this specialization has developed independently in the different orders to resolve a common environmental or behavioral need and is not due to shared evolutionary ancestry. It remains to be assessed whether this parallel evolutionary trait is associated with an overall two-dimensional movement through the environment in rodents versus a 3D movement ecology as seen in bats and primates. It would thus be interesting to record from DG in flying bats, and to compare 3D neural representations in the two blades of DG: because the two blades receive different patterns of projections from LEC and MEC, they might show different functional properties, for example, 2D coding in one blade and 3D coding in the other.

ACKNOWLEDGMENTS

We thank Avishag Tuval and Maya Weinberg for veterinary support and Bruno Monterotti for assistance with sectioning and histological processing of parts of the material. This study was supported in part by a grant from the European Research Council to N.U. (ERC-StG—NEUROBAT), the Kimmel Award for Innovative Investigation to N.U., the Centre of Excellence scheme of the Norwegian Research Council—Centre for neural computation (grant 223262), and the Kavli Foundation.

CONFLICT OF INTEREST STATEMENT

The authors declare that the research was conducted without any commercial or financial relationships that could be a potential conflict of interest.

DATA AVAILABILITY STATEMENT

The experimental data will be made available as digital scans upon reasonable request.

ORCID

Heidi Kleven https://orcid.org/0000-0002-3710-321X
Menno P. Witter https://orcid.org/0000-0003-0285-1637

REFERENCES

Amaral, D. G., Dolorfo, C., & Alvarez-Royo, P. (1991). Organization of CA1 projections to the subiculum: A PHA-L analysis in the rat. *Hippocampus*, *1*(4), 415–435. https://doi.org/10.1002/hipo.450010410

Amaral, D. G., & Lavenex, P. (2007). Hippocampal neuroanatomy. In P. Andersen, R. Morris, D. G. Amaral, T. Bliss, & J. O'Keefe (Eds.), *The hippocampus book* (pp. 37–114). Oxford University Press.

Buhl, E. H., & Dann, J. F. (1991). Cytoarchitecture, neuronal composition, and entorhinal afferents of the flying fox hippocampus. *Hippocampus*, *1*(2), 131–152. https://doi.org/10.1002/hipo.450010203

Collitti-Klausnitzer, J., Hagena, H., Dubovyk, V., & Manahan-Vaughan, D. (2021). Preferential frequency-dependent induction of synaptic depression by the lateral perforant path and of synaptic potentiation by the medial perforant path inputs to the dentate gyrus. *Hippocampus*, *31*(9), 957–981. https://doi.org/10.1002/hipo.23338

Cotter, J. R., & Laemle, L. K. (1990). Cholecystokinin (CCK)-like immunoreactivity in the brain of the little brown bat (Myotis lucifugus). *Journal für Hirnforschung*, *31*(1), 87–97.

Deshmukh, S. S., & Knierim, J. J. (2011). Representation of non-spatial and spatial information in the lateral entorhinal cortex. *Frontiers in Behavioral Neuroscience*, *5*, 69. https://doi.org/10.3389/fnbeh.2011.00069

Eilam-Altstadter, R., Las, L., Witter, M. P., & Ulanovsky, N. (2022). *Stereotaxic brain atlas of the Egyptian fruit bat*. Academic Press. https://doi.org/10.1016/C2021-0-02649-3

Finkelstein, A., Derdikman, D., Rubin, A., Foerster, J. N., Las, L., & Ulanovsky, N. (2015). Three-dimensional head-direction coding in the bat brain. *Nature*, *517*(7533), 159–164. https://doi.org/10.1038/nature14031

Finkelstein, A., Las, L., & Ulanovsky, N. (2016). 3-D maps and compasses in the brain. *Annual Review of Neuroscience*, *39*, 171–196. https://doi.org/10.1146/annurev-neuro-070815-013831

Flasbeck, V., Atucha, E., Nakamura, N. H., Yoshida, M., & Sauvage, M. M. (2018). Spatial information is preferentially processed by the distal part of CA3: Implication for memory retrieval. *Behavioural Brain Research*, *354*, 31–38. https://doi.org/10.1016/j.bbr.2018.07.023

Gatome, C. W., Slomianka, L., Mwangi, D. K., Lipp, H. P., & Amrein, I. (2010). The entorhinal cortex of the Megachiroptera: A comparative study of Wahlberg's epauletted fruit bat and the straw-coloured fruit bat. *Brain Structure & Function*, *214*(4), 375–393. https://doi.org/10.1007/s00429-010-0239-z

Ginosar, G., Aljadeff, J., Burak, Y., Sompolinsky, H., Las, L., & Ulanovsky, N. (2021). Locally ordered representation of 3D space in the entorhinal cortex. *Nature*, *596*(7872), 404–409. https://doi.org/10.1038/s41586-021-03783-x

Hafting, T., Fyhn, M., Molden, S., Moser, M. B., & Moser, E. I. (2005). Microstructure of a spatial map in the entorhinal cortex. *Nature*, *436*(7052), 801–806. https://doi.org/10.1038/nature03721

Hjorth-Simonsen, A. (1972). Projection of the lateral part of the entorhinal area to the hippocampus and fascia dentata. *The Journal of Comparative Neurology*, *146*(2), 219–232. https://doi.org/10.1002/cne.901460206

Hjorth-Simonsen, A., & Jeune, B. (1972). Origin and termination of the hippocampal perforant path in the rat studied by silver impregnation. *The Journal of Comparative Neurology*, *144*(2), 215–232. https://doi.org/10.1002/cne.901440206

Høydal, Ø. A., Skytøen, E. R., Andersson, S. O., Moser, M. B., & Moser, E. I. (2019). Object-vector coding in the medial entorhinal cortex. *Nature*, *568*(7752), 400–404. https://doi.org/10.1038/s41586-019-1077-7

Ino, T., Kaneko, T., & Mizuno, N. (1998). Direct projections from the entorhinal cortical layers to the dentate gyrus, hippocampus, and subicular complex in the cat. *Neuroscience Research*, *32*(3), 241–265. https://doi.org/10.1016/s0168-0102(98)00093-5

Insausti, R., Herrero, M. T., & Witter, M. P. (1997). Entorhinal cortex of the rat: Cytoarchitectonic subdivisions and the origin and distribution of cortical efferents. *Hippocampus*, *7*(2), 146–183. https://doi.org/10.1002/(SICI)1098-1063(1997)7:2<146::AID-HIPO4>3.0.CO;2-L

Keene, C. S., Bladon, J., McKenzie, S., Liu, C. D., O'Keefe, J., & Eichenbaum, H. (2016). Complementary functional organization of neuronal activity patterns in the perirhinal, lateral entorhinal, and medial entorhinal cortices. *The Journal of Neuroscience*, *36*(13), 3660–3675. https://doi.org/10.1523/jneurosci.4368-15.2016

Maass, A., Berron, D., Libby, L. A., Ranganath, C., & Duzel, E. (2015). Functional subregions of the human entorhinal cortex. *eLife*, *4*, e06426. https://doi.org/10.7554/eLife.06426

Moser, M. B., Rowland, D. C., & Moser, E. I. (2015). Place cells, grid cells, and memory. *Cold Spring Harbor Perspectives in Biology*, *7*(2), a021808. https://doi.org/10.1101/cshperspect.a021808

Naber, P. A., Lopes da Silva, F. H., & Witter, M. P. (2001). Reciprocal connections between the entorhinal cortex and hippocampal fields CA1 and the subiculum are in register with the projections from CA1 to the subiculum. *Hippocampus*, *11*(2), 99–104. https://doi.org/10.1002/hipo.1028

Nakamura, N. H., Flasbeck, V., Maingret, N., Kitsukawa, T., & Sauvage, M. M. (2013). Proximodistal segregation of nonspatial information in CA3: Preferential recruitment of a proximal CA3-distal CA1 network in nonspatial recognition memory. *The Journal of Neuroscience*, *33*(28), 11506–11514. https://doi.org/10.1523/JNEUROSCI.4480-12.2013

O'Keefe, J., & Dostrovsky, J. (1971). The hippocampus as a spatial map. Preliminary evidence from unit activity in the freely-moving rat. *Brain Research*, *34*(1), 171–175. https://doi.org/10.1016/0006-8993(71)90358-1

Pettigrew, J. D., Jamieson, B. G., Robson, S. K., Hall, L. S., McAnally, K. I., & Cooper, H. M. (1989). Phylogenetic relations between microbats, megabats and primates (Mammalia: Chiroptera and Primates). *Philosophical Transactions of the Royal Society of London. Series B, Biological Sciences*, *325*(1229), 489–559. https://doi.org/10.1098/rstb.1989.0102

Ritchey, M., Libby, L. A., & Ranganath, C. (2015). Cortico-hippocampal systems involved in memory and cognition: The PMAT framework. *Progress in Brain Research*, *219*, 45–64. https://doi.org/10.1016/bs.pbr.2015.04.001

Savelli, F., Yoganarasimha, D., & Knierim, J. J. (2008). Influence of boundary removal on the spatial representations of the medial entorhinal cortex. *Hippocampus*, *18*(12), 1270–1282. https://doi.org/10.1002/hipo.20511

Šimić, G., Krsnik, Ž., Knezović, V., Kelović, Z., Mathiasen, M. L., Junaković, A., Radoš, M., Mulc, D., Španić, E., Quattrocolo, G., Hall, V. J., Zaborszky, L., Vukšić, M., Bordonau, F. O., Kostović, I., Witter, M. P., & Hof, P. R. (2022). Prenatal development of the human entorhinal cortex. *The Journal of Comparative Neurology*, *530*, 1–38. https://doi.org/10.1002/cne.25344

Solstad, T., Boccara, C. N., Kropff, E., Moser, M. B., & Moser, E. I. (2008). Representation of geometric borders in the entorhinal cortex. *Science*, *322*(5909), 1865–1868. https://doi.org/10.1126/science.1166466

Springer, M. S., Stanhope, M. J., Madsen, O., & de Jong, W. W. (2004). Molecules consolidate the placental mammal tree. *Trends in Ecology & Evolution*, *19*(8), 430–438. https://doi.org/10.1016/j.tree.2004.05.006

Tamamaki, N. (1997). Organization of the entorhinal projection to the rat dentate gyrus revealed by DiI anterograde labeling. *Experimental Brain Research*, *116*(2), 250–258. https://doi.org/10.1007/pl00005753

Tamamaki, N., & Nojyo, Y. (1993). Projection of the entorhinal layer II neurons in the rat as revealed by intracellular pressure-injection of neurobiotin. *Hippocampus*, *3*(4), 471–480. https://doi.org/10.1002/hipo.450030408

Tamamaki, N., & Nojyo, Y. (1995). Preservation of topography in the connections between the subiculum, field CA1, and the entorhinal cortex in rats. *The Journal of Comparative Neurology*, *353*(3), 379–390. https://doi.org/10.1002/cne.903530306

Tsagkogeorga, G., Parker, J., Stupka, E., Cotton, J. A., & Rossiter, S. J. (2013). Phylogenomic analyses elucidate the evolutionary relationships of bats. *Current Biology*, *23*(22), 2262–2267. https://doi.org/10.1016/j.cub.2013.09.014

Tsao, A., Moser, M. B., & Moser, E. I. (2013). Traces of experience in the lateral entorhinal cortex. *Current Biology*, *23*(5), 399–405. https://doi.org/10.1016/j.cub.2013.01.036

Tsao, A., Sugar, J., Lu, L., Wang, C., Knierim, J. J., Moser, M. B., & Moser, E. I. (2018). Integrating time from experience in the lateral entorhinal cortex. *Nature*, *561*(7721), 57–62. https://doi.org/10.1038/s41586-018-0459-6

van Groen, T., Miettinen, P., & Kadish, I. (2003). The entorhinal cortex of the mouse: Organization of the projection to the hippocampal formation. *Hippocampus*, *13*(1), 133–149. https://doi.org/10.1002/hipo.10037

van Strien, N. M., Cappaert, N. L. M., & Witter, M. P. (2009). The anatomy of memory: An interactive overview of the parahippocampal–hippocampal network. *Nature Reviews Neuroscience*, *10*(4), 272–282. https://doi.org/10.1038/nrn2614

Witter, M. P. (1989). Connectivity of the rat hippocampus. In V. Chan-Palay & C. Köhler (Eds.), *The hippocampus-new vistas* (Vol. 52, pp. 53–69). Allen R. Liss.

Witter, M. P. (2007). The perforant path: Projections from the entorhinal cortex to the dentate gyrus. *Progress in Brain Research*, *163*, 43–61. https://doi.org/10.1016/S0079-6123(07)63003-9

Witter, M. P., & Amaral, D. G. (1991). Entorhinal cortex of the monkey: V. Projections to the dentate gyrus, hippocampus, and subicular complex. *The Journal of Comparative Neurology*, *307*(3), 437–459. https://doi.org/10.1002/cne.903070308

Witter, M. P., Doan, T. P., Jacobsen, B., Nilssen, E. S., & Ohara, S. (2017). Architecture of the entorhinal cortex a review of entorhinal anatomy in rodents with some comparative notes. *Frontiers in Systems Neuroscience*, *11*, 46. https://doi.org/10.3389/fnsys.2017.00046

Witter, M. P., Kleven, H., & Kobro Flatmoen, A. (2017). Comparative contemplations on the hippocampus. *Brain, Behavior and Evolution*, *90*(1), 15–24. https://doi.org/10.1159/000475703

Witter, M. P., Van Hoesen, G. W., & Amaral, D. G. (1989). Topographical organization of the entorhinal projection to the dentate gyrus of the monkey. *The Journal of Neuroscience*, *9*(1), 216–228.

Wyss, J. M. (1981). An autoradiographic study of the efferent connections of the entorhinal cortex in the rat. *The Journal of Comparative Neurology*, *199*(4), 495–512. https://doi.org/10.1002/cne.901990405

Yartsev, M. M., & Ulanovsky, N. (2013). Representation of three-dimensional space in the hippocampus of flying bats. *Science*, *340*(6130), 367–372. https://doi.org/10.1126/science.1235338

Yartsev, M. M., Witter, M. P., & Ulanovsky, N. (2011). Grid cells without theta oscillations in the entorhinal cortex of bats. *Nature*, *479*(7371), 103–107. https://doi.org/10.1038/nature10583

SUPPORTING INFORMATION

Additional supporting information can be found online in the Supporting Information section at the end of this article.

How to cite this article: Jacobsen, B., Kleven, H., Gatome, W., Las, L., Ulanovsky, N., & Witter, M. P. (2023). Organization of projections from the entorhinal cortex to the hippocampal formation of the Egyptian fruit bat *Rousettus aegyptiacus*. *Hippocampus*, *33*(8), 889–905. https://doi.org/10.1002/hipo.23517